

Iterative optical technique for detecting anti-leishmania nanoparticles in mouse lesions

INBAR YARIV,^{1,2} SRIRAM KANNAN,^{2,3} YIFAT HAREL,^{2,4} ESTHY LEVY,^{2,4} HAMOOTAL DUADI,^{1,2} JEAN-PAUL LELLOUCHE,^{2,4} SHULAMIT MICHAELI,^{2,3} AND DROR FIXLER^{1,2,*} 

¹Faculty of Engineering, Bar Ilan University, Ramat Gan 5290002, Israel

²The Institute of Nanotechnology and Advanced Materials, Bar Ilan University, Ramat Gan 5290002, Israel

³The Mina and Everard Goodman Faculty of Life Sciences, Bar Ilan University, Ramat Gan 5290002, Israel

⁴Department of Chemistry Faculty of Exact Sciences, Bar Ilan University, Ramat Gan 5290002, Israel

*Dror.Fixler@biu.ac.il

Abstract: Nanoparticles (NPs) based drugs for topical administration are gaining interest in the biomedical world. However, a study tool of their penetration depth to the different tissue layers without additional markers or contrast agents is required in order to relieve safety concerns. While common diagnostic tools, e.g. X-ray, computed tomography or magnetic resonance imaging, can provide *in vivo* detection of the metallic NPs, their resolution cannot determine the exact penetration depth to the thin skin layers. In this work, we propose the noninvasive nanophotonics iterative multi-plane optical property extraction (IMOPE) technique for the novel iron-based NPs detection in leishmaniasis lesions. The optical properties of the different tissue layers: epidermis, dermis, subcutaneous fat and muscle, were examined before and after topical drug administration. The potential topical drug was detected in the epidermis ($\sim 13\mu\text{m}$) and dermis ($\sim 160\mu\text{m}$) layers in mice lesions at different stages of the disease (two or four weeks post infection). The lesion size influence on the detection was also observed, where in larger lesions the IMOPE senses a greater presence of the topical drug.

© 2021 Optical Society of America under the terms of the [OSA Open Access Publishing Agreement](#)

1. Introduction

Leishmaniasis, caused by parasites from the *Leishmania* type, is spread by sandflies bites. This tropical disease, which affects millions of people around the world, exists in three forms: mucosal leishmaniasis (ML); cutaneous leishmaniasis (CL); and visceral leishmaniasis (VL) [1]. Approximately 75% of CL cases are found in north Africa, South America and Asia, including the middle east [2]. CL is the most common form, associated with skin lesions with a very long healing process that leave scars. Currently, there is no vaccine for any of these diseases and the drugs available are either very expensive, have side effects or the parasites develop resistance to them [1]. Hence, it is necessary to develop a drug that will treat this disease effectively, specifically cream based to avoid painful local injections, or systemic toxic treatments.

Recently, a research regarding the development of a drug for leishmaniasis has obtained quite encouraging effective results [3]. That research presented a potential topical drug that is based on innovative nanoscale cerium (III-IV) cation/complex-doped maghemite nanoparticles (NPs) [3–5] that were coordinatively attached to 25 kDa branched polyethyleneimine (PEI) polymer to create positively charged nanocarriers [3,5,6]. These positive PEI-maghemite NPs delivered to the parasite single lysosome, causing a “proton sponge” effect which leads to water intake and then to lysosome rupture [7]. The fact that the *Leishmania* has only one lysosome is why the NPs are cytolytic to it and causing the death of the parasite. This nano-drug named Nano-Leish-IL was tested as a topical treatment using varying bases (cream, ointment, gel or suspension) on lesions of mice infected with *Leishmania major*. The effectivity of the PEI-maghemite NPs alone, the cream as a base and their combination were examined to verify the drug activity [3].

The Nano-Leish-IL as a topical treatment was found to eliminate the development of lesions containing parasites by ~90%. It is a stable nano-drug and no drug resistance was observed. Nonetheless, as with any new drug or cosmetic product that are applied topically, the NPs penetration to the deeper layers of the skin arises a concern, which had to be tested and clarified by appropriate scientific investigation.

With nanomedicine becoming a key player in the field of drug delivery, detection of NPs *in vivo* became necessary for ensuring they reached their destination and examining their functionality mechanism [8,9]. The NPs penetration ability to the skin depends on their characteristics such as size, shape and surface chemistry [10–12]. For safety reasons, it is necessary also to assess the possible penetration of the drug to the blood from its site of administration.

Metallic NPs detection *in vivo* is done constantly using known imaging modalities, such as computed tomography (CT) or magnetic resonance imaging (MRI), where their high atomic number makes them powerful contrast agents [13–18]. Both modalities, CT and MRI, combined with metallic NPs can produce high resolution *in vivo* images of different organs. However, for the detection in different layers of the skin, their resolution is limited, and hence other techniques are required. Optical coherence tomography (OCT) is known as an optical imaging technique that can produce high resolution images of thin samples [19]. The idea of using inorganic NPs, e.g. gold NPs [20–22] and metal oxide NPs [23–25] for increasing the contrast of the images has recently been utilized in OCT as well. Those metallic NPs are mostly used for increasing image resolution rather than being the objects for detection. Histopathology is a very common technique for examining different skin layers [26–28], enabling the detection of diseases, lesions and NPs in the tissue [26,29]. It is able to produce microscopic images of the tissue with high resolution, nevertheless, this technique is destructive to the tissue being examined. Hence, *in vivo* examination of the skin tissue is not optional using histopathology. Another approach in detection of drug delivery in skin studies is fluorescence-based techniques based on either a fluorescent drug or fluorescently tagged nanocarriers [30,31]. These techniques detect the drug either by monitoring the fluorescence intensity or its lifetime using fluorescence lifetime imaging microscopy (FLIM) [9,15,30–32]. However, in case of the latter, where the nanocarrier is fluorescently tagged, the additional fluorophore might affect the drug penetration to the skin layers, which may result in misdetection.

This study aims to examine the Nano-Leish-IL penetration to the skin layers of the lesions by a noninvasive optical technique called the iterative multi-plane optical property extraction (IMOPE) [33–40]. The IMOPE is a noninvasive nanophotonics technique, which extracts the scattering properties of an irradiated substance based on its reconstructed reemitted light phase. The presence of NPs in the different skin layers should affect the scattering properties and enable the NPs detection. The IMOPE technique records light intensity images at different positions using an experimental setup. The intensity images are then used by the iterative Gerchberg-Saxton (GS) algorithm [41] for reconstructing the phase that was lost once the images were captured. Having reconstructed the phase image, a quantitative criterion, specifically the root mean square, is calculated from a chosen spatial region in the phase image, in order to extract the scattering properties of the sample. We have recently utilized the IMOPE multi-layer study [40] for the *in vivo* detection of different layers. In this study, the IMOPE multi-layer study is utilized for detecting the Nano-Leish-IL penetration to a mouse epidermis, dermis, subcutaneous fat, and muscle layers. First, the optical fingerprint of the Nano-Leish-IL NPs was tested in the IMOPE technique by adding the NPs to tissue-like phantoms. Then, three groups of mice were examined, at different stages of the disease, before applying the Nano-Leish-IL and following the drug application. The phase images were reconstructed and the phase RMS for the different layers was calculated based on the layer's known scattering properties. The IMOPE results indicate the Nano-Leish-IL presence in the epidermis and dermis layers of the infected mice, which predicts the drug's ability to effectively penetrate the lesions of the *Leishmania* causing the CT disease.

2. Material and methods

2.1. The IMOPE technique

The IMOPE technique, as mentioned above, extracts the scattering properties based on the reemitted light phase. The technique is constructed based on three fundamental components combined together: (1) the phase retrieval GS algorithm [41]; (2) the experimental setup; and (3) a theoretical model. The theoretical model forms the connection between the reduced scattering coefficient of a medium and its reemitted light phase. The IMOPE theoretical model is based on the steady-state diffusion reflection (DR) [42–44] and the master-slave dual-source configuration [45] as described in detail in [39]. The IMOPE works as follows (Fig. 1): first light intensity images are captured in the experimental setup. These images are then used for reconstructing the reemitted light phase by the multi-plane GS algorithm (the process is described fully in [37]). Once the phase is reconstructed, a quantitative criterion, the RMS, of its distribution is calculated based on the following equation:

$$RMS_{\varphi_M} = \frac{\sqrt{\sum_{x,y \in \gamma} |A_M(x,y)e^{i\varphi_M(x,y)} - A_M(x,y)e^{i\bar{\varphi}_M}|^2}}{\sqrt{\sum_{x,y} |A_M(x,y)|^2}} \quad (1)$$

where $\varphi_M(x,y)$ is the reconstructed phase accumulated at the desired plane following a propagation distance of $dz^*(M-1)$. M is the number of planes and dz is the distance between every two planes. $A_M(x,y)$ and $\bar{\varphi}_M$ are the amplitude and the average phase at the desired M^{th} plane along the optical axis z respectively, and γ is the spatial region of interest (ROI).

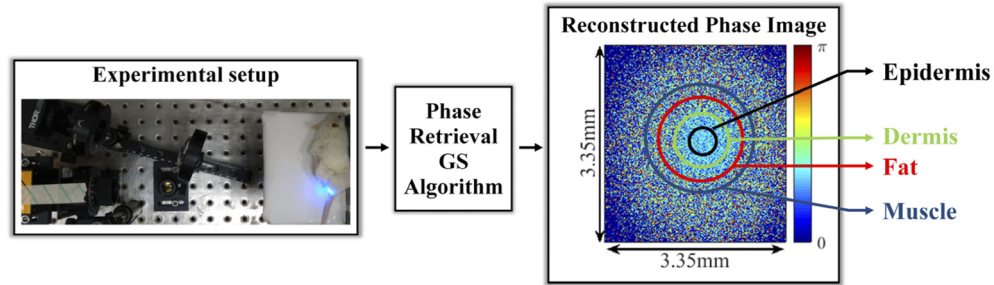


Fig. 1. A schematic description of the IMOPE technique. It starts with the experimental setup for recording light intensity images. These images are processed by the GS algorithm for reconstructing the phase image. Next, the RMS (Eq. (1)) is computed from a chosen spatial region of interest (ROI) in the phase image. The ROI is either the outside or the inside of a circular border that represents the multiple ($r > \text{MFP}'$) or single ($r < \text{MFP}'$) scattering regimes respectively. This circular border, MFP' , is correlated with the scattering properties of the sample. Having four thin layers in the sample, we focused on the single scattering regime ($r < \text{MFP}'$). Each phase image contains four circles, where each represents the ROI for a specific tissue layer: epidermis, dermis, fat and muscle (as marked on the phase image).

We have previously presented the spatial ROIs in the phase images [36–39]. The ROIs can be either the area inside or outside a circle. The circle radius is correlated with the scattering properties of the sample (specifically the reduced scattering coefficient, μ_s') and is defined by the mean free path transport ($\text{MFP}' = 1/\mu_s'$). The area where $r < \text{MFP}'$, also known as the single scattering regime, focuses at the closer range and lower penetration depths. Whereas the area where $r > \text{MFP}'$, known to be the multiple scattering regime, represents higher penetration depths. For the *in vivo* study here, the ROIs were chosen based on the different layers we wished to detect as presented in Fig. 1. Since these layers are very thin we have focused on the single

scattering regime, *i.e.* $r < \text{MFP}'$. The computed phase RMS is in direct relation with the scattering properties of the sample, which change with tissue type, presence of additional materials etc.

Single-layer media have two spatial ROIs ($r < \text{MFP}'$ and $r > \text{MFP}'$) in the phase image, which are related theoretically to their scattering. This idea was recently expanded to multi-layer samples. Each scattering layer creates a set of single and multiple scattering regimes that are separated by a border correlated to the scattering property of the layer. In this case, where N layers are taken into account, each phase image contains $2N$ spatial regions that translate to $2N$ scattering regimes. This paradigm was presented in our latest study on two-layer solid tissue-like phantoms, where for each phantom four spatial ROIs were taken into account [40].

2.1.1. Detection of different mouse tissue layers

In order to analyze the IMOPE results, we first conducted a literature search for optical properties of mouse tissues and their thicknesses. The mouse skin tissue contains three layers of the epidermis ($\sim 13\mu\text{m}$), dermis ($\sim 160\mu\text{m}$) and subcutaneous fat ($\sim 170\mu\text{m}$) [46]. Following the three skin layers, there is a successive muscle layer. The related optical properties, for $\lambda=475\text{nm}$, specifically the reduced scattering coefficient (μ_s') of different tissues are details in Table 1 [47]. In this study, four tissue layers are examined: the epidermis, the dermis, the subcutaneous fat (refer to as fat) and muscle. The different skin layers we examined are very thin, hence the phase RMS was calculated only from the single scattering regime ($r < \text{MFP}'$). The MFP' of the four layers are presented (in pixels) in Table 1. By this method, in one phase image in a specific scan, we can analyze different layers (as presented in Fig. 1).

Table 1. Optical properties of different tissue layers of a mouse in the blue wavelength.

	Epidermis	Dermis	Subcutaneous fat	Muscle
μ_s' [mm^{-1}]	3.2	2.3	1.5	1.15
MFP' [pixel]	40	80	130	170

2.1.2. Experimental setup

In order to record light intensity images at different locations, the reflection-based IMOPE experimental setup was built. The experimental setup is composed of a laser source, polarizers, a lens and a camera (Fig. 2(a)). The laser source is a diode-pumped solid-state (DPSS, MBL-III473, ReadyLasers) laser with a wavelength of $\lambda=473\text{nm}$ and attenuated power of 1mW. The polarizers (LPVISE100-A, Thorlabs, Japan) were added for clearing the surface reflection [48]. The polarizers were perpendicular to one another with the first one positioned to receive the maximum intensity. The lens, with a focal length of $f=75\text{mm}$, was set to focus the light beam (with a magnification of 1) to the CMOS camera (DCC1545M, Thorlabs, Japan). The lens, polarizer and camera were set on a motorized micrometer stage (PT1-Z8, Thorlabs, Japan) in order to record the light images at different positions along the z -axis with equal intervals, dz , between them. The motorized stage was placed at a 14.5° from the laser; therefore the images were corrected accordingly. The mice (control and infected corresponding to (Fig. 2(b) and (c) respectively) were set on a plate held on a three-axis micrometer stage (PT3, Thorlabs, Japan) for any x - y - z adjustments.

2.2. Nano-Leish-IL

2.2.1. Materials

The chemicals and reagents; $\text{FeCl}_3 \cdot 6\text{H}_2\text{O}$, $\text{FeCl}_2 \cdot 4\text{H}_2\text{O}$, NH_4OH (ACS reagent, 28–30%), ceric ammonium nitrate (CAN), and 25 kDa branched polyethylenimine (PEI) were purchased from

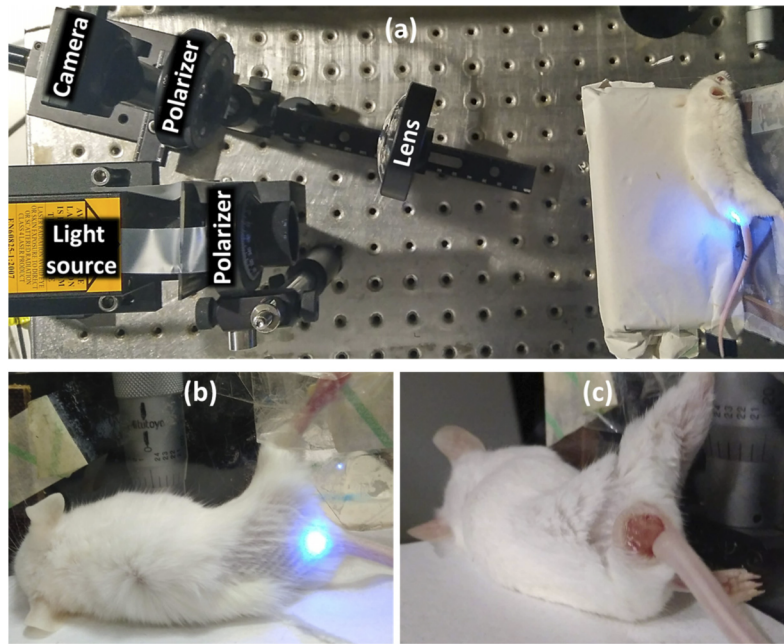


Fig. 2. (a) The IMOPE experimental setup for recording the reflected light intensity images. The images are recorded at multiple z locations, with a distance of dz between them. The light source is a DPSS laser with a wavelength of $\lambda=473$ nm and an attenuated power of 1 mW. The lens, with a focal length of $f=75$ mm, focuses the light on the camera (with a magnification of 1). Polarizers were used for optical clearing purposes. The lens, polarizer and camera are set on a motorized micrometer stage with an angle of 14.5° . The mice are set on a plate held by a three-axis micrometer stage for adjustments in the x - y - z directions. The mice under the laser irradiation (b) control and (c) infected, were irradiated on the same location at the top of the tail, where the lesions are located.

Sigma-Aldrich (Rehovot, Israel) and were used without any further purification. The face cream “Revive Me Deep Replenishing Serum” was purchased from FRÉ Brand, Israel.

2.2.2. PEI-maghemite NPs fabrication

The fabrication of PEI-maghemite NPs involved three steps (Fig. 3(a)). The first two steps described in previous publications [3,4,49] and include the preparation of magnetite NPs (Fe_2O_3) and then the iron oxidation to maghemite NPs (Fe_3O_4) using Ceric Ammonium Nitrate (CAN). The oxidation take place under ultrasonication (Sonics, Vibra cell 750) resulting with Ce cation/complex doping on the maghemite NPs surface. The third step is the coordination attachment of 25 kDa branched PEI to the $\text{Ce}^{3/4+}$ -doped-maghemite NPs. In this step, an aqueous solution of 25 kDa branched PEI (10 mg/ml) was added to a diluted NPs suspension (to a final Fe concentration of 0.082 mg/ml, and with a PEI/Fe weight ratio of 6.7) and placed for 48 hours at 15°C in an orbital shaker (200 rpm). The resulting crude product was washed 3 times with ddH₂O using centrifugation with an Amicon Ultra-15 centrifugal filter device (100 K), followed by two size exclusion process (8,000 and 7,000 rpm) as detailed in our previous publication [3].

2.2.3. NPs characterization

In order to study the structure and size of the NPs, a Transmission Electron Microscopy (TEM), JEOL 1400 at 120 kV, JEOL JEM-2100 (LaB6) at 200 kV was used. The TEM samples were

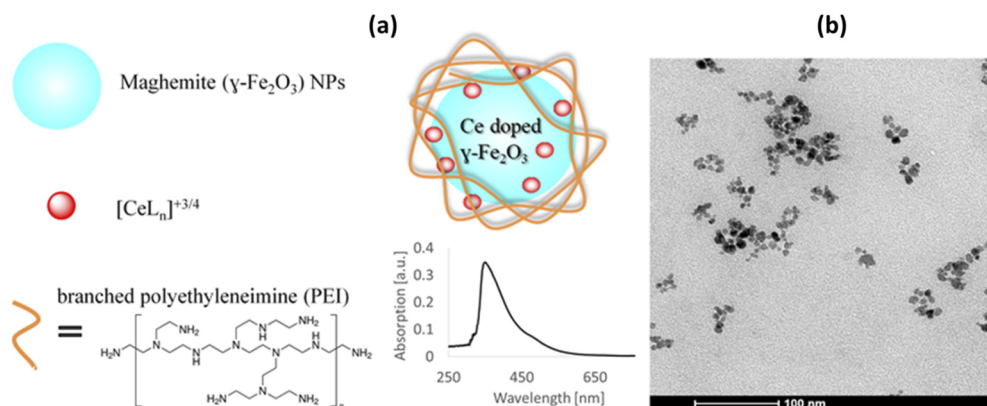


Fig. 3. (a) Illustration of the PEI-maghemite NPs and their absorption spectrum. The PEI-maghemite NPs components: the maghemite NPs are obtained by oxidation of the Fe in the magnetite NPs. The maghemite NPs are then doped by Ce^{3+/4+} cations/complexes and attached to 25KDs branched PEI to obtain the PEI-maghemite NPs. (b) TEM image of the PEI-maghemite NPs.

prepared on an amorphous carbon-coated copper grid (Formvar carbon 400 mesh grids, SPI Supplies West Chester, PA, USA). The average diameter of the PEI-maghemite NPs was found to be 9.76 ± 1.79 nm and determined by measuring 100 NPs based on TEM images (Fig. 3(b)).

In addition, Zetasizer Nano-ZS (Malvern Instruments Ltd, Malvern, UK) was used for measuring both Dynamic Light Scattering (DLS) for hydrodynamic average diameter and ζ potential of PEI-maghemite NPs [operating with 5 mW He-Ne laser (633 nm, 20 °C), using disposable DTS1060C-Cleare ζ cells (ddH₂O, 25 °C)]. These measurements revealed DLS sizes of 70-90 nm with good polydispersity (PDI: 0.18–0.207), and positive ζ potential of +25-35 mV. UV-VIS spectra was obtained on a Cary 100 Bio UV-VIS spectrometer (Agilent Technologies, Santa Clara, CA, US) and presented in Fig. 3(a). The Fe concentration of the final PEI-maghemite NPs dispersion measured by ICP (ICP-OES) analyses, carried out using a FHX22 MultiView plasma (SOP, EOP), (Horiba [Jobin-Yvon division], Kyoto, Japan).

2.2.4. Preparation of the NPs in cream

In this study, we prepared the Nano-Leish-IL cream with a 0.067% w/w of Fe, which connects 0.5% of the total Nano-Leish-IL drug. The NPs solution was diluted in water and added gradually (while mixing) to the “Revive Me Deep Replenishing Serum” face cream (FRÉ Brand, Israel), at a 2:1 water to cream volume ratio. The final formulation was then mixed for one additional minute using a vortex until a uniform texture was obtained.

2.3. Tissue-like phantom experiments

In order to examine the Nano-Leish-IL optical signature, first only the Fe NPs were measured using the IMOPE technique. The Fe NPs were measured using a liquid tissue-like phantom as a scattering base. Tissue-like phantoms are used constantly to optically mimic different tissues with their component concentrations dictating the phantom’s final scattering and absorption properties [18,50]. The scattering component used was IntraLipid (IL) (IntraLipid 20% Emulsion, Sigma-Aldrich, Israel). The IL was mixed with ddH₂O for receiving a concentration of 1% IL, which translates to $\mu_s' = 1.77\text{mm}^{-1}$ for $\lambda=473\text{nm}$ [38]. The Fe NPs were added to the liquid phantom giving a final concentration of 0.2%Fe. The solutions were transferred to cuvettes that set on a 3-axis manual micrometer stage for fine-tuning during experiments [51].

2.4. In vivo experiments

In vivo experiments were conducted on three groups of mice: 1. Uninfected control mice; 2. Mice 2 weeks post *Leishmania* infection with small lesions (will be referred to as group 2); 3. Mice 4 weeks post *Leishmania* infection with big lesions (will be referred to as group 3). The mice were measured under the IMOPE at four time points: before treatment with the cream and then 1, 3 and 6 hours following the cream application.

The *Leishmania* infection was on the mice tail base, hence the mice laid on a flat surface with their tail facing the laser, as presented in Fig. 2 (the hair was removed pre-measurements). Each mouse was placed on a sample holder, set on a 3-axis manual micrometer stage for fine-tuning during experiments, and fixed to the polycarbonate mount. The surface of the mouse skin was kept perpendicular to the direction of the incident laser beam through the experiments.

2.4.1. Animal infection and maintenance

Specific pathogen free BALB/c female mice of age 8-9 weeks were used and were maintained in SPF conditions all through the experiment. For establishing infection in the tail base of mice, subcutaneous tail base injections with *Leishmania major* (Friedlin strain) 1×10^7 cells were done in the animal house facility. Mice were randomly assigned to uninfected control and infected cohorts. The mice were maintained in cages that have 12hour light-dark cycle at room temperature and fed with a standard rodent diet and ad libitum access to food and water.

This study was approved by the head of Bar Ilan University animal studies ethical committee with study approval no 01.01.2018. All mice experiments were performed according to the guidelines set by the Institutional care and use of research animals of Bar Ilan University. All measurements were performed under anesthesia by intraperitoneal injections of ketamine-xylazine mix with a dose appropriate to their body weight. After completion of Laser measurement, mice were sacrificed using CO₂.

3. Results

3.1. Detection of the Fe NPs optical signature in phantom

In order to detect the Nano-Leish-IL penetration to the skin layers, first the optical signal of the Fe NPs had to be validated by the IMOPE technique. Initial examination was performed as detailed in section 2.3. The 473nm laser was chosen since the NPs have an optical signature in the blue regime, as presented by their absorption spectrum in Fig. 3(a). The NPs concentration examined was very low for safety reasons (0.2%Fe) and as they are mostly absorbing, they were inserted to a liquid phantom which acted as a scattering base to the NPs as in the skin environment. For each sample, three measurements were done using the experimental setup (Fig. 2(a)). The light intensity images were recorded at different locations along the depth dimension (z-axis) with $dz=635\mu\text{m}$. The phase was reconstructed by applying the multi-plane GS algorithm (as detailed in [37]), using 4 successive intensity images at the size of 3.35mm X 3.35mm, (total propagation distance of 1.9mm). In order to preserve the circular symmetry of the radiation source, a threshold condition was incorporated in the phase images. As explained above, for a homogenous single layer the phase RMS is computed from two ROIs: the inside and outside of a circular border, where the radius based on the layer's scattering property. The liquid phantoms had a scattering property of $\mu_s'=1.77\text{mm}^{-1}$, which translates to a radius of 0.56mm (108 pixels). Figure 4 presents the phase RMS calculated from the single scattering regime (the inside of the circular border) at the surface of the liquid phantom without (black bar) and with 0.2%Fe NPs (red bar). The change in the RMS value is clearly visible, which indicates the IMOPE ability to detect the Fe NPs in spite of their low scattering ability. Note, that in our previous studies [36–40], for the single scattering regime we have presented a decrease in the RMS value as the scattering increases. However, here, adding the NPs to the liquid phantom caused an opposite

behavior, an increase rather than decrease in the phase RMS due to the NPs higher absorption ability than scattering.

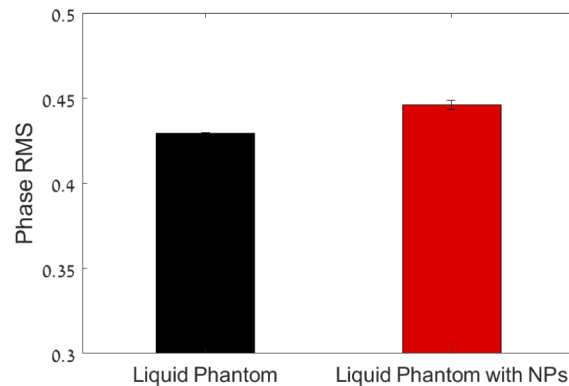


Fig. 4. Detecting the optical signal of the Fe NPs in a liquid phantom. The obtained phase RMS at the surface of a liquid phantom (black bar) and with an additional 0.2%Fe NPs (red bar). The liquid phantom was prepared with 1% IL translating to $\mu_s' = 1.77^{-1} \text{ mm}$. The phase RMS was calculated from the single scattering regime, the inside of the circular border with a radius of 0.56 mm. The phase was reconstructed using 4 successive intensity images with a $dz = 0.635 \mu\text{m}$ distance between them.

3.2. Nano-Leish-IL penetration in *in vivo* model

In vivo measurements of the mice were performed using the IMOPE experimental setup (Fig. 2(a)) as detailed in section 2.3, and the mice were positioned with their tail's bases facing the laser (Fig. 2(b) and (c)). For each mouse, 3 measurements were done at each time point. Intensity images were recorded at different locations along the depth dimension (z -axis) with $dz = 635 \mu\text{m}$. All parameters for the phase reconstruction were kept as detailed above at the phantom experiments. However, the analysis of the phase image was adjusted for *in vivo* measurements. For each phase image, the phase RMS was computed from four ROIs as detailed above (section 2.1.1). The phase RMS calculated from the control mouse is presented in Fig. 5(a) based on the different tissue layers (epidermis, dermis, fat and muscle corresponds to their colored circles on Fig. 5(b)). Figure 5(b) presents an example of the absolute value of the phase image reconstructed at the surface of a mouse with the ROIs marked on it. The ROIs are the encircled areas, where each circle (black, green, red and blue) corresponds to a different tissue layer (epidermis, dermis, fat and muscle respectively) and its radius is according to the detailed information in Table 1. For each tissue type, we examined the computed RMS, in the single scattering regime, before applying the cream (triangles in Fig. 5(a)) and 3 hours after (squares in Fig. 5(a)). The control mouse results, for all layers, indicate there is no change before and after the cream was applied, meaning that the cream and NPs remained on the skin surface only and didn't penetrate deeper.

We continued to examine the infected mice. The same analysis was performed on the infected mice and the results are presented in Fig. 6. As with the control mouse, the different tissue layers (epidermis, dermis, fat and muscle presented in Fig. 6(a)-(d) respectively) are represented by the different radii (corresponding to 40, 80, 130, and 170 pixels). In each figure, the different time points: before, 1 hour, 3 hours, and 6 hours after applying the cream correspond to triangles, rhombuses, circles and stars. For all layers, the phase RMS exhibits an increase following the cream application (1h, 3h and 6h in comparison to before). Looking specifically at the epidermis (Fig. 6(a)) and dermis (Fig. 6(b)), after applying the cream (1h, 3h and 6h), this increase is followed by a decrease in their RMS values along the depth scanning. Their RMS values decrease

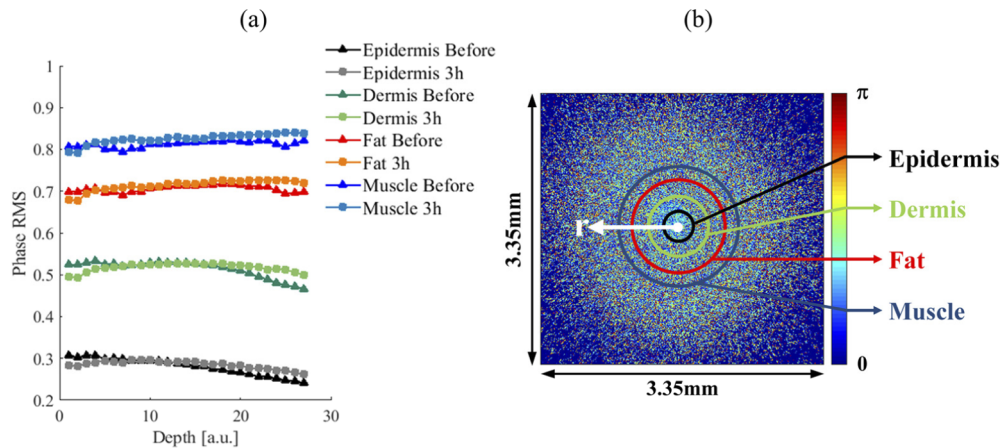


Fig. 5. The control group phase RMS computed along the depth dimension (z axis) for different tissue layers. (a) The phase RMS from the epidermis (black), dermis (green), fat (red) and muscle (blue), before (triangles) and 3 h after (squares) applying the cream is presented. For each tissue layer, the phase RMS was calculated based on the ROIs presented in (b). (b) A reconstructed phase image and the different ROIs marked on it. On each phase image, the RMS was computed from four spatial ROIs which are the circles marked on the image. The ROIs radius was set according to the scattering properties of the four tissue layers: epidermis, dermis, fat and muscle (corresponding to the black, green, red and blue circles marked on the phase image). This phase image was reconstructed at the surface of a mouse before applying the cream.

towards the RMS curve received before applying the cream (triangle). This decrease indicates the depth point where the tissue layer behaves as before the NPs were applied. The combination of the RMS increase followed by its decrease back to the control level act as a sign of the presence of the NPs in the epidermis and dermis layers. The presence of the NPs creates a change in the optical properties of the tissues that translates to higher RMS values compared to before applying the cream (triangles). Hence the increase of the RMS is a result of the drug that was applied. The decrease back to the control curve at the deeper part of the epidermis and dermis layers shows that at that area the tissue has no NPs and act as the control curve. However, when examining the fat (Fig. 6(c)) and muscle (Fig. 6(d)) layers, the phase RMS along the depth scanning, after applying the cream (1h, 3h and 6h), does not decrease but rather stays higher than the RMS before (black triangle). This indicates that there is no presence of the NPs in these layers.

Finally, the phase RMS results from mice at the later stage of the disease (with the larger lesions) are presented in Fig. 7. The phase RMS, for the epidermis, dermis, fat, and muscle layers (Fig. 7(a)-(d) respectively) at the different time points (which are represented by the different curves as detailed in Fig. 6) was computed based on the ROIs presented in Fig. 5(b). The behavior of the RMS curves for the epidermis (Fig. 7(a)) and dermis (Fig. 7(b)) are similar to the ones seen in small lesions, meaning the curves increase and then decrease back to the curve before applying the cream (triangles) as we advance in the depth dimension. These results indicate the presence of the NPs in these layers. For the other tissue layers (fat and muscle presented in Fig. 7(c) and (d) respectively), the RMS values don't decrease towards the RMS before applying the cream, which means the cream was not detected there. Note that for this group the curves after applying the cream have a larger dynamic range and the different time points can be visually separated. This is mainly due to the fact that the big lesions enable better penetration to the skin layers.

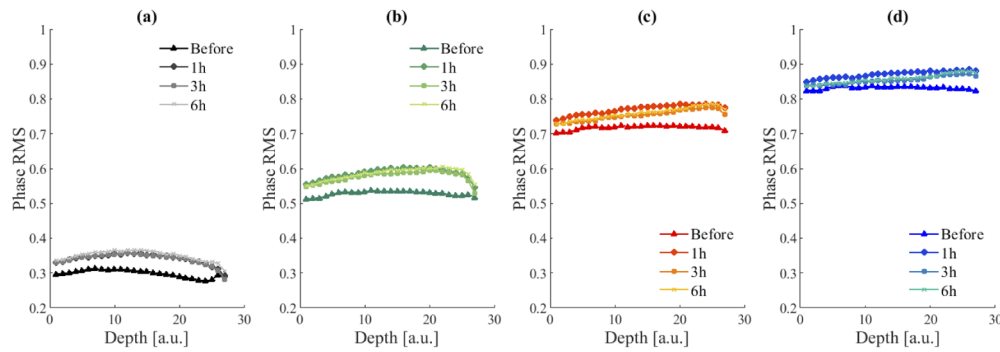


Fig. 6. Phase RMS of small lesions computed along the z axis (the depth dimension) for different tissue layers. The RMS from the (a) epidermis, (b) dermis, (c) fat and (d) muscle was calculated based on the ROI presented in Fig. 5(b) (corresponding to 40, 80, 130 and 170 pixels respectively). The different curves in each figure represent the different time periods: before, 1 h, 3 h and 6 h after the cream was applied correspond to triangles, rhombuses, circles and stars.

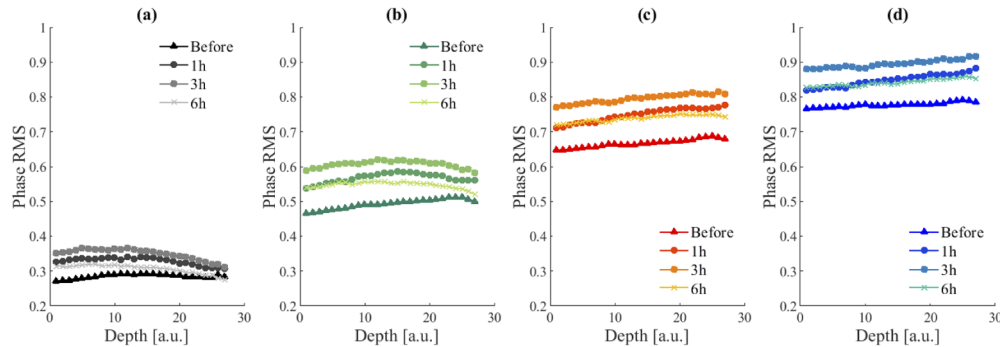


Fig. 7. Phase RMS of big lesions computed along the z axis (the depth dimension) for different tissue layers. The RMS from the (a) epidermis, (b) dermis, (c) fat and (d) muscle are represented by 40, 80, 130 and 170 pixel respectively. The different curves represent the different time periods: before, 1 h, 3 h and 6 h after the cream was applied correspond to triangles, rhombuses, circles and stars.

4. Discussion

The aim of this work was to examine the skin penetration of the recently developed Nano-Leish-IL drug [3], using the IMOPE technique. The IMOPE technique extracts the optical properties of different substances based on the remitted light phase that is reconstructed by the GS algorithm. The quantitative criterion of the phase, its RMS, is calculated from chosen spatial ROIs in the reconstructed phase images, where the ROI sizes correlate to the optical properties of the sample. In order to sense the NPs in the IMOPE, the 473nm laser was chosen as a radiation source due to the NPs optical activity mainly in the blue regime, as can be seen in the absorption spectrum in Fig. 3(a). Since we wished to detect the particles in quite thin mouse skin, we chose the wavelength regime where they have an optical signature, knowing it will allow lower penetration. In this study, first the optical signature of the Fe NPs in the Nano-Leish-IL was examined in liquid phantoms with a scattering base of $\mu_s' = 1.77\text{mm}^{-1}$ and ROI with a radius of 0.56mm ($=1/\mu_s'$). Having the ability to sense the NPs by the IMOPE, *in vivo* measurements were performed. There, the chosen ROIs radii were according to the different tissue layers (epidermis, dermis,

subcutaneous fat and muscle). The results presented above (Fig. 6 and Fig. 7) indicated the penetration ability of the NPs to the epidermis and dermis layers for the infected mice (small and big lesions). However, we wished to compare the influence of the lesion size on the skin penetration ability. For that, the phase RMS value obtained before the cream application (Before in Fig. 5, Fig. 6, and Fig. 7) was subtracted from the one obtained 3h after (3h in the same figures) for all three groups (Fig. 8). The phase RMS difference is presented for each of the layers (epidermis, dermis, fat and muscle) in Fig. 8(a)-(d) respectively. The control group (dash line), the healthy mice, represents the threshold line. For this group, looking at the different layers there seems to be no change while advancing deeper into the skin layers (dash line in Fig. 8(a)-(d)), suggesting that no NPs were detected in the different layers but rather left on the surface of the skin. Examination of the phase RMS difference of the infected mice (small and big lesions corresponding to circles and triangles) produces a clear influence of the lesion size on the amount of the detected NPs. The higher values in the graph represent the greater presence of the NPs in the tissues. However, it is not only the higher values detected but also the change in the curves shape while advancing deeper in the layers. Looking at the small lesions (circles), the curve seems to increase mainly while advancing from the epidermis to the dermis (Fig. 8(a) and (b)), which indicates the NPs reached both layers. The big lesions (triangles), however, present an increase in the curves while advancing from the epidermis all the way to the fat layer (Fig. 8(a)-(c)), demonstrating the presence of NPs in all those layers. This comparison shows that in the larger lesions, we can sense greater changes following the cream application.

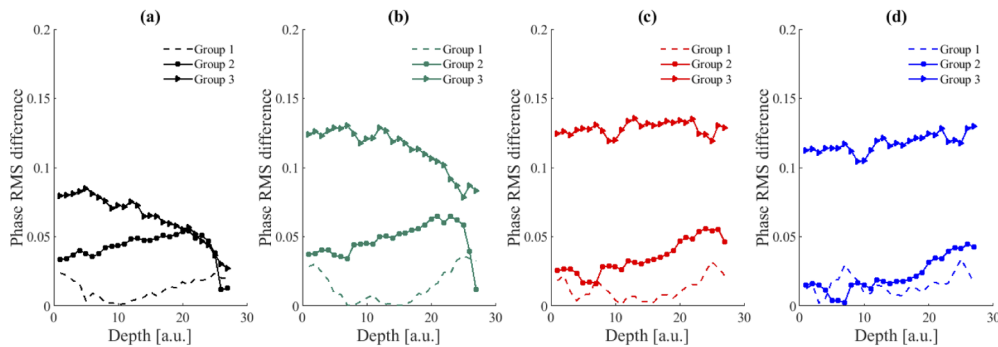


Fig. 8. The change in the phase RMS 3 hours following the cream application in comparison to before. The phase RMS difference for the (a) epidermis (b) dermis (c) fat and (d) muscle layers obtained for the control group (dashed line), for small lesions (circles) and for big lesions (triangles).

Note that a phenomenon we have noticed along the results presented above (Fig. 6 and Fig. 7), is that while the phase RMS increases with time (from before through 1h and up to 3h after applying the cream), 6h following the cream application we observe a decrease in its values. We will have to further investigate this phenomenon in order to understand the diffusion and clearance mechanism of the NPs from the lesion area. Clearance of metallic NPs from the infected area within hours has been reported previously [27], and could provide an insight to the Fe NPs behavior in the *in vivo* model and how we should design the treatment with Nano-Leish-IL. It is important to note that mice skin differ from the human skin in terms of thickness and optical properties. Where human skin is around few millimeters the mouse skin thickness is around few hundreds of micrometers, hence the NPs penetration depth to human skin may change and should be further examined.

5. Conclusion

In vivo detection of metallic NPs is achieved by diagnostic tools such as CT and MRI. However, these techniques are limited in terms of resolution when wishing to separate the different skin layers. In order to detect *in vivo* NPs within skin layers, usually optical techniques are used in combination with contrast agents. Though, additional contrast agents may disrupt the penetration ability of the NPs. This paper presented the use of the noninvasive nanophotonics reflection-based IMOPE technique for optically detecting the Nano-Leish-IL NPs in skin layers of mice infected with *Leishmania major*. The IMOPE technique detects the scattering properties of a medium using a quantitative criterion of the reconstructed light phase as an indicator. The technique reconstructs the light phase using the GS algorithm and calculates the phase RMS from chosen spatial ROIs in the phase image. The spatial ROIs are the inside or outside of a circular border that is correlated with the scattering properties of the sample. In this study, the detection of NPs presence within 4 different layers: epidermis, dermis, fat and muscle, is presented, based on the multi-layer analysis of the IMOPE, using four ROIs correlated to the scattering properties of the layers. Following an initial examination for detecting the Fe NPs optical signature by the IMOPE, *in vivo* measurements were performed on mice. Three groups were tested: uninfected and infected mice at two different stages of the disease (with small and big lesions). The phase RMS results present the ability of the reflection-based IMOPE to detect the NPs presence and estimate their skin penetration ability to the different layers, specifically to the epidermis and dermis. Moreover, comparing the results received from different time points post treatment (3h following in comparison to before applying the cream), may suggest the preferential timing for administration of the drug. The lesion size also influenced the penetration depth, suggesting the ability of the drug to penetrate and reach parasites beyond the site of administration.

Disclosures. The authors have no conflicts of interest to disclose.

Data availability. Data underlying the results presented in this paper are not publicly available at this time but may be obtained from the authors upon reasonable request.

References

1. M. Ghorbani and R. Farhoudi, "Leishmaniasis in humans: drug or vaccine therapy?" *Drug Des., Dev. Ther.* **12**, 25–40 (2017).
2. D. Savoia, "Recent updates and perspectives on leishmaniasis," *J. Infect. Dev. Countries* **9**(06), 588–596 (2015).
3. S. Kannan, Y. Harel, E. Levy, A. Dolitzky, A. E. Sagiv, S. Aryal, L. Suleman, J.-P. Lellouche, and S. Michaeli, "Nano-Leish-IL: A novel iron oxide-based nanocomposite drug platform for effective treatment of cutaneous leishmaniasis," *J. Controlled Release* **335**, 203–215 (2021).
4. L. L. Israel, E. Lellouche, R. S. Kenett, O. Green, S. Michaeli, and J.-P. Lellouche, "Ce 3/4+ cation-functionalized maghemite nanoparticles towards siRNA-mediated gene silencing," *J. Mater. Chem. B* **2**(37), 6215–6225 (2014).
5. S. M. Jean-Paul Lellouche, Liron LimorIsrael, Yifat Harel, Avishay Dolitzky, and Stella Ostrovsky, "Core-shell particles comprising metal oxide and lanthanide element," (2019).
6. L. L. Israel, E. Lellouche, S. Ostrovsky, V. Yarmiayev, M. Bechor, S. Michaeli, and J.-P. Lellouche, "Acute *in vivo* toxicity mitigation of PEI-coated maghemite nanoparticles using controlled oxidation and surface modifications toward siRNA delivery," *ACS Appl. Mater. Interfaces* **7**(28), 15240–15255 (2015).
7. O. Boussif, F. Lezoualc'h, M. A. Zanta, M. D. Mergny, D. Scherman, B. Demeneix, and J.-P. Behr, "A versatile vector for gene and oligonucleotide transfer into cells in culture and *in vivo*: polyethylenimine," *Proc. Natl. Acad. Sci.* **92**(16), 7297–7301 (1995).
8. A. Zvyagin, X. Zhao, A. Gierden, W. Sanchez, J. Ross, and M. Roberts, "Imaging of zinc oxide nanoparticle penetration in human skin *in vitro* and *in vivo*," *J. Biomed. Opt.* **13**(6), 064031 (2008).
9. V. R. Leite-Silva, M. L. Lamer, W. Y. Sanchez, D. C. Liu, W. H. Sanchez, I. Morrow, D. Martin, H. D. T. Silva, T. W. Prow, J. E. Grice, and M. S. Roberts, "The effect of formulation on the penetration of coated and uncoated zinc oxide nanoparticles into the viable epidermis of human skin *in vivo*," *Eur. J. Pharm. Biopharm.* **84**(2), 297–308 (2013).
10. J. Lademann, H. Richter, A. Teichmann, N. Otberg, U. Blume-Peytavi, J. Luengo, B. Weiss, U. F. Schaefer, C.-M. Lehr, and R. Wepf, "Nanoparticles—an efficient carrier for drug delivery into the hair follicles," *Eur. J. Pharm. Biopharm.* **66**(2), 159–164 (2007).
11. H. I. Labouta and M. Schneider, "Interaction of inorganic nanoparticles with the skin barrier: current status and critical review," *Nanomedicine* **9**(1), 39–54 (2013).

12. P. Dong, F. F. Sahle, S. B. Lohan, S. Saeidpour, S. Albrecht, C. Teutloff, R. Bodmeier, M. Unbehauen, C. Wolff, and R. Haag, "pH-sensitive Eudragit® L 100 nanoparticles promote cutaneous penetration and drug release on the skin," *J. Controlled Release* **295**, 214–222 (2019).
13. R. Weissleder, P. F. Hahn, D. D. Stark, E. Rummeny, S. Saini, J. Wittenberg, and J. T. Ferrucci, "MR imaging of splenic metastases: ferrite-enhanced detection in rats," *AJR, Am. J. Roentgenol.* **149**(4), 723–726 (1987).
14. C. Alexiou, W. Arnold, P. Hulin, R. J. Klein, H. Renz, F. G. Parak, C. Bergemann, and A. S. Lübbe, "Magnetic mitoxantrone nanoparticle detection by histology, X-ray and MRI after magnetic tumor targeting," *J. Magn. Magn. Mater.* **225**(1-2), 187–193 (2001).
15. M. S. Roberts, Y. Dancik, T. W. Prow, C. A. Thorling, L. L. Lin, J. E. Grice, T. A. Robertson, K. König, and W. Becker, "Non-invasive imaging of skin physiology and percutaneous penetration using fluorescence spectral and lifetime imaging with multiphoton and confocal microscopy," *Eur. J. Pharm. Biopharm.* **77**(3), 469–488 (2011).
16. M. Shilo, T. Reuveni, M. Motiei, and R. Popovtzer, "Nanoparticles as computed tomography contrast agents: current status and future perspectives," *Nanomedicine* **7**(2), 257–269 (2012).
17. X. Liu, L. Liu, X. Hu, S. Zhou, R. Ankri, D. Fixler, and Z. Xie, "Multimodal bioimaging based on gold nanorod and carbon dot nanohybrids as a novel tool for atherosclerosis detection," *Nano Res.* **11**(3), 1262–1273 (2018).
18. R. Ankri, S. Melzer, A. Tarnok, and D. Fixler, "Detection of gold nanorods uptake by macrophages using scattering analyses combined with diffusion reflection measurements as a potential tool for in vivo atherosclerosis tracking," *Int J Nanomedicine* **10**, 4437–4446 (2015).
19. A. G. Podoleanu, "Optical coherence tomography," *Br. J. Radiol.* **78**(935), 976–988 (2005).
20. T. S. Troutman, J. K. Barton, and M. Romanowski, "Optical coherence tomography with plasmon resonant nanorods of gold," *Opt. Lett.* **32**(11), 1438–1440 (2007).
21. D. C. Adler, S.-W. Huang, R. Huber, and J. G. Fujimoto, "Photothermal detection of gold nanoparticles using phase-sensitive optical coherence tomography," *Opt. Express* **16**(7), 4376–4393 (2008).
22. C. S. Kim, P. B. Wilder-Smith, Y.-C. Ahn, L.-H. L. Liaw, Z. Chen, and Y. J. Kwon, "Enhanced detection of early-stage oral cancer in vivo by optical coherence tomography using multimodal delivery of gold nanoparticles," *J. Biomed. Opt.* **14**(3), 034008 (2009).
23. A. L. Oldenburg, V. Crecea, S. A. Rinne, and S. A. Boppart, "Phase-resolved magnetomotive OCT for imaging nanomolar concentrations of magnetic nanoparticles in tissues," *Opt. Express* **16**(15), 11525–11539 (2008).
24. R. Z. Seeni, X. Yu, H. Chang, P. Chen, L. Liu, and C. Xu, "Iron oxide nanoparticle-powered micro-optical coherence tomography for in situ imaging the penetration and swelling of polymeric microneedles in the skin," *ACS Appl. Mater. Interfaces* **9**(24), 20340–20347 (2017).
25. A. Indoliya, M. Mohan, P. Kharey, S. Gupta, and R. Poddar, "Polymerically modified superparamagnetic iron oxide nanoparticles as a multi-model molecular probe for functionalized optical coherence tomography," *Opt. Laser Technol.* **141**, 107108 (2021).
26. T. Krenacs, I. Zsakovics, T. Micsik, L. Fonyad, S. V. Varga, L. Ficsor, G. Kiszler, and B. Molnar, "Digital microscopy: the upcoming revolution in histopathology teaching, diagnostics, research and quality assurance," *Microscopy: Science, Technology, Applications and Education* **2**, 965–977 (2010).
27. A. Hirshberg, I. Allon, I. Novikov, R. Ankri, A. Ashkenazy, and D. Fixler, "Gold nanorods reflectance discriminate benign from malignant oral lesions," *Nanomedicine* **13**(4), 1333–1339 (2017).
28. D. Fixler, R. Ankri, I. Kaplan, I. Novikov, and A. Hirshberg, "Diffusion reflection: a novel method for detection of oral cancer," *J. Dent. Res.* **93**(6), 602–606 (2014).
29. S. Sudri, H. Duadi, F. Altman, I. Allon, A. Ashkenazy, R. Chakraborty, I. Novikov, D. Fixler, and A. Hirshberg, "Diffusion reflection method for early detection of oral squamous cell carcinoma specifically targeted by circulating gold-nanorods bio-conjugated to anti-epidermal growth factor receptor," *Int. J. Nanomed.* **16**, 2237–2246 (2021).
30. H.-S. Cho, Z. Dong, G. M. Pauletti, J. Zhang, H. Xu, H. Gu, L. Wang, R. C. Ewing, C. Huth, F. Wang, and D. Shi, "Fluorescent, superparamagnetic nanospheres for drug storage, targeting, and imaging: a multifunctional nanocarrier system for cancer diagnosis and treatment," *ACS Nano* **4**(9), 5398–5404 (2010).
31. U. Alexiev, P. Volz, A. Boreham, and R. Brodewolf, "Time-resolved fluorescence microscopy (FLIM) as an analytical tool in skin nanomedicine," *Eur. J. Pharm. Biopharm.* **116**, 111–124 (2017).
32. D. Fixler, R. Tirosh, N. Zurgil, and M. Deutsch, "Tracing apoptosis and stimulation in individual cells by fluorescence intensity and anisotropy decay," *J. Biomed. Opt.* **10**(3), 034007 (2005).
33. I. Yariv, G. Rahamim, E. Shliselberg, H. Duadi, A. Lipovsky, R. Lubart, and D. Fixler, "Detecting nanoparticles in tissue using an optical iterative technique," *Biomed. Opt. Express* **5**(11), 3871–3881 (2014).
34. I. Yariv, Y. Kapp-Barnea, E. Genzel, H. Duadi, and D. Fixler, "Detecting concentrations of milk components by an iterative optical technique," *J. Biophotonics* **8**(11-12), 979–984 (2015).
35. I. Yariv, M. Haddad, H. Duadi, M. Motiei, and D. Fixler, "New optical sensing technique of tissue viability and blood flow based on nanophotonic iterative multi-plane reflectance measurements," *Int. J. Nanomed.* **11**, 5237–5244 (2016).
36. I. Yariv, H. Duadi, and D. Fixler, "Optical method to extract the reduced scattering coefficient from tissue: theory and experiments," *Opt. Lett.* **43**(21), 5299–5302 (2018).
37. I. Yariv, H. Duadi, R. Chakraborty, and D. Fixler, "Algorithm for in vivo detection of tissue type from multiple scattering light phase images," *Biomed. Opt. Express* **10**(6), 2909–2917 (2019).
38. I. Yariv, C. Shapira, H. Duadi, and D. Fixler, "media characterization under scattering conditions by nanophotonics iterative multiplane spectroscopy measurements," *ACS Omega* **4**(10), 14301–14306 (2019).

39. I. Yariv, H. Duadi, and D. Fixler, "An optical method to detect tissue scattering: theory, experiments and biomedical applications," in *SPIE BiOS*, (SPIE, 2019).
40. I. Yariv, H. Duadi, and D. Fixler, "Depth scattering characterization of multi-layer turbid media based on iterative multi-plane reflectance measurements," *IEEE Photonics J.* **12**(5), 1–13 (2020).
41. R. W. Gerchberg and W. O. Saxton, "A practical algorithm for the determination of phase image and diffraction plane pictures," *Optik* **35**, 237–246 (1972).
42. T. J. Farrell, M. S. Patterson, and B. Wilson, "A diffusion theory model of spatially resolved, steady-state diffuse reflectance for the noninvasive determination of tissue optical properties in vivo," *Med. Phys.* **19**(4), 879–888 (1992).
43. D. Piao, R. L. Barbour, H. L. Graber, and D. C. Lee, "On the geometry dependence of differential pathlength factor for near-infrared spectroscopy. I. Steady-state with homogeneous medium," *J. Biomed. Opt.* **20**(10), 105005 (2015).
44. R. Ankri, H. Taitelbaum, and D. Fixler, "On Phantom experiments of the photon migration model in tissues," *Open Opt. J.* **5**(1), 28–32 (2011).
45. D. Piao and S. Patel, "Simple empirical master-slave dual-source configuration within the diffusion approximation enhances modeling of spatially resolved diffuse reflectance at short-path and with low scattering from a semi-infinite homogeneous medium," *Appl. Opt.* **56**(5), 1447–1452 (2017).
46. C. P. Sabino, A. M. Deana, T. M. Yoshimura, D. F. da Silva, C. M. França, M. R. Hamblin, and M. S. Ribeiro, "The optical properties of mouse skin in the visible and near infrared spectral regions," *J. Photochem. Photobiol., B* **160**, 72–78 (2016).
47. G. Alexandrakakis, F. R. Rannou, and A. F. Chatziioannou, "Tomographic bioluminescence imaging by use of a combined optical-PET (OPET) system: a computer simulation feasibility study," *Phys. Med. Biol.* **50**(17), 4225–4241 (2005).
48. V. V. Tuchin, L. Wang, and D. A. Zimnyakov, *Optical Polarization in Biomedical Applications* (Springer Science & Business Media, 2006).
49. E. Haimov-Talmoud, Y. Harel, H. Schori, M. Motiei, A. Atkins, R. Popovtzer, J.-P. Lellouche, and O. Shefi, "Magnetic targeting of mTHPC to improve the selectivity and efficiency of photodynamic therapy," *ACS Appl. Mater. Interfaces* **11**(49), 45368–45380 (2019).
50. R. Cubeddu, A. Pifferi, P. Taroni, A. Torricelli, and G. Valentini, "Experimental test of theoretical models for time-resolved reflectance," *Med. Phys.* **23**(9), 1625–1633 (1996).
51. D. Fixler, J. Garcia, Z. Zalevsky, A. Weiss, and M. Deutsch, "Pattern projection for subpixel resolved imaging in microscopy," *Micron* **38**(2), 115–120 (2007).